Interaction of a Fin Trailing Vortex
with a Downstream Control Surface

Steven J. Beresh,[*] Justin A. Smith,[†] John F. Henfling,[‡] Thomas W. Grasser,[§] and Russell W. Spillers[¶]
Sandia National Laboratories, Albuquerque, NM, 87185

A sub-scale experiment has been constructed using fins mounted on one wall of a transonic wind tunnel to investigate the influence of fin trailing vortices upon downstream control surfaces. Data are collected using a fin balance instrumenting the downstream fin to measure the aerodynamic forces of the interaction, combined with stereoscopic Particle Image Velocimetry to determine vortex properties. The fin balance data show that the response of the downstream fin essentially is shifted from the baseline single-fin data dependent upon the angle of attack of the upstream fin. Freestream Mach number and the spacing between fins have secondary effects. The velocimetry shows that the vortex strength increases markedly with upstream fin angle of attack, though even an uncanted fin generates a noticeable wake. No variation with Mach number can be discerned in the normalized velocity data. Correlations between the force data and the velocimetry suggest that the interaction is fundamentally a result of an angle of attack superposed upon the downstream fin by the vortex shed from the upstream fin tip. The Mach number influence arises from differing vortex lift on the leading edge of the downstream fin even when the impinging vortex is Mach invariant.

Introduction

As a result of the precision-guidance capabilities found on many modern missiles and bombs, the complexity of the aerodynamic control surfaces is increasing as many vehicles now combine the presence of fins with strakes or canards. Consequently, the tip vortices shed from the upstream control surfaces propagate downstream where they can interact with subsequent control surfaces and dramatically alter their expected performance, an interaction for which neither the knowledge base nor the predictive modeling is adequately developed. The severity of this interaction can be extreme, sometimes leading to an inability to control the vehicle at all, much less with the great precision for which it was intended.

Such fin-wake interactions often are addressed by conducting wind tunnel tests on specific flight configurations, then deriving aerodynamic models that can be used by the guidance system. Clearly, this approach is inefficient due to the need for new data following every design change, and the use of reliable predictive tools to minimize the testing requirements is greatly preferable. Although a number of engineering-level predictive methods exist (for example, [1, 2]), they are hampered by the difficult challenge of accurately predicting the vortices shed by control surfaces across a wide range of flow conditions and geometric variations. Higher-fidelity CFD predictions may be attempted, but generate considerable computational expense as well as questions regarding the accuracy of their results. Regardless of the computational tool, it must be validated against reliable experimental data for the regime in which it will be applied, but some studies have indicated that common predictive codes, despite some impressive successes, may exhibit significant deficiencies for guided-missile geometries [2-5].

---

[*]Principal Member of the Technical Staff, Engineering Sciences Center, Senior Member AIAA, correspondence to: P.O. Box 5800, Mailstop 0825, (505) 844-4618, email: sjberes@sandia.gov
[†]Member of the Technical Staff, Member AIAA.
[‡]Distinguished Technologist, Member AIAA.
[§]Distinguished Technologist.
[¶]Senior Technologist

To approach this problem, an experimental program is underway in Sandia's Trisonic Wind Tunnel (TWT) to study the vortex shed from a fin installed on a wall of the tunnel and its impingement upon a second fin placed downstream of the first. The wind tunnel wall represents the surface of a hypothetical flight vehicle rather than employing a traditional sting-mounted model of a missile body, so that a reasonably sized flowfield may be produced in a smaller facility. Data on the structure of the wake of the upstream fin are measured using Particle Image Velocimetry (PIV), coupled with downstream fin force and moment instrumentation using a specialized balance to determine its altered aerodynamic performance. Such a data set can be used to develop and validate computational models within the flight regime of interest to Sandia for precision-guidance flight hardware.

Fig. 1: Sketch of the fin geometry. Dimensions in mm.

Experimental Apparatus
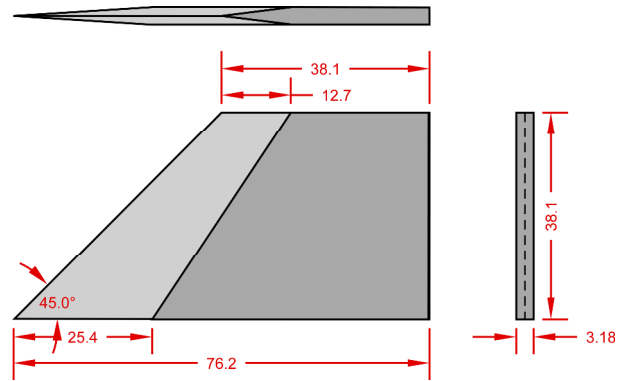
Trisonic Wind Tunnel

Experiments were performed in Sandia's Trisonic Wind Tunnel (TWT), which is a blowdown-to-atmosphere facility using air as the test gas through a 305×305 mm^2 (12×12 inch^2) rectangular test section enclosed within a pressurized plenum. Several test section configurations are possible using either porous walls to alleviate the transonic choking condition or solid walls for subsonic compressible conditions. The solid-wall transonic test section was used for the present work rather than the traditional ventilated

Fig. 2: Fins mounted to the top wall of the test section, with the downstream fin attached to a fin balance.

version because it offers reasonable optical access, a flat plate upon which models may be mounted from the wall, and computationally tractable boundary conditions for comparison of experimental data and numerical simulations. The use of a solid-wall test section limits the Mach number range of the flowfield, but this was considered an acceptable compromise.
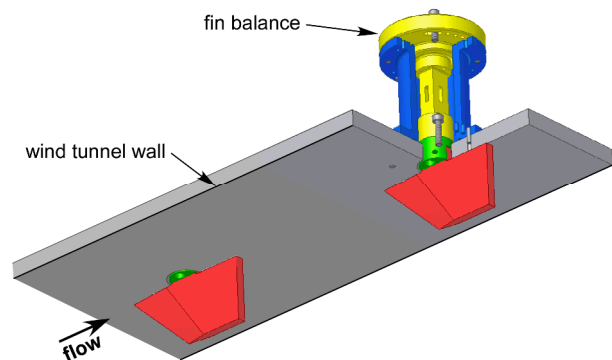
Fin Hardware

The data presented in the current report use a single design for both fins, shown in Fig. 1, as a generic representation of the various fin geometries that could be found on actual flight systems. Based upon a trapezoidal planform, the leading edge sweep is 45°, the fin root chord 76.2 mm (3 inch), the fin span 38.1 mm (1.5 inch), and its thickness 3.18 mm (0.125 inch). The sharp leading edge has a taper that terminates at a length of 1/3 the chord. Fins were fabricated from stainless steel to guard against aeroelastic deformation and black oxide coated to reduce background light scatter for the PIV measurements.

Each fin attaches to either the fin balance or a low-profile dummy balance, passing through the test section wall using a hub-and-pin system. This is shown in Fig. 2 with the downstream fin attached to the balance, which is described below. Both the balance and the dummy balance mount can be set to discrete angles of attack ranging from -5° to +10° in 1° increments, pinned in place to tightly-toleranced positions to promote repeatability. The center of rotation is the midpoint of the fin root. A gap of 1.5 mm (0.06 inch) exists between the root of the fin and the wind tunnel wall.
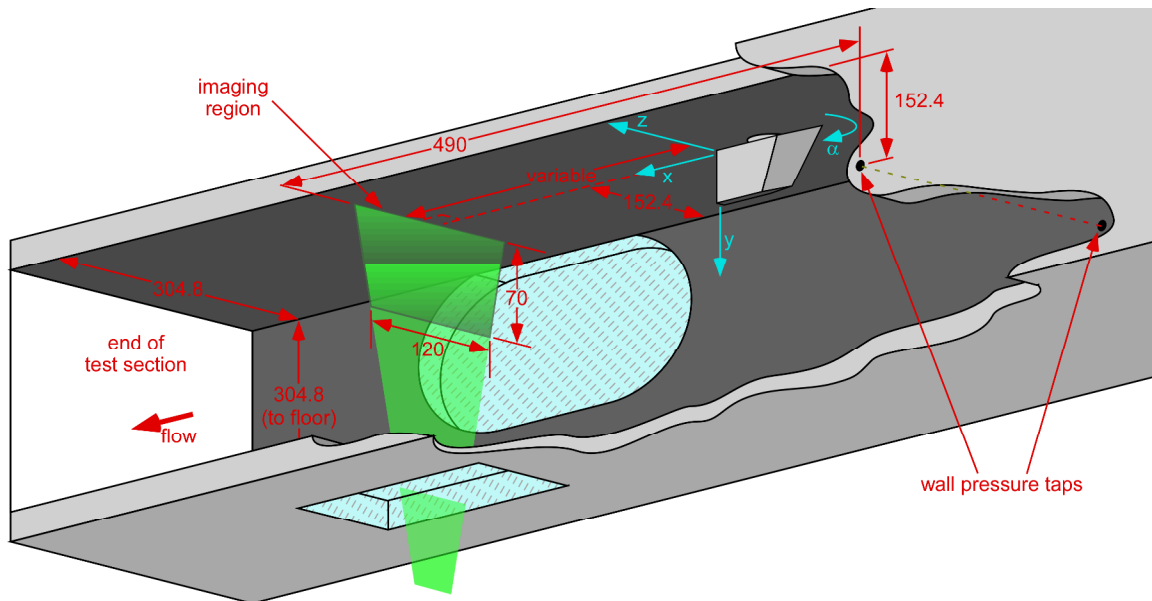
The axial position of each fin is adjustable within a range of 457 mm (18.0 inch) using a series of interchangeable sliding mounting blocks within a rail cut into the test section wall. Some limitations are placed upon the fin position when connected to the balance due to interference from the tunnel infrastructure behind the wall, but the dummy balance is of sufficiently small stature that it fits anywhere. Repositioning the fins between wind tunnel runs allows an examination of the spacing between fins as an experimental parameter, in combination with adjusting the angles of attack of each fin.

Fig. 3: Schematic of the crossplane configuration for PIV measurements, looking in the downstream direction from below the test section. Flow is from right to left. All dimensions are in millimeters. Not to scale.

Fin Force Balance

The customized fin balance used in the present study was procured from Allied Aerospace's Force Measurement Systems division and is capable of measuring three components: the fin normal force, the bending moment, and the hinge moment; owing to the relatively thin fin size, the axial force is assumed to be negligible. A maximum load of 220 N (50 lbs-force) normal force is possible. The design is essentially the same as a strain-gage internal balance routinely used in aerodynamic testing. The balance aligns along the fin axis of rotation and is mounted behind the wind tunnel wall, as shown in Fig. 2, using a cylindrical housing. The balance rotates within the canister along with the fin when adjusted to different angles of attack with respect to the oncoming flow. The mechanism to set the fin angle is attached to the rear of the balance and operates as described above.

The balance was calibrated by adapting it to a system normally used for calibrating internal balances and replacing the fin with a loading plate that allows calibration weights to be hung. The combination of different loading positions and weight magnitudes could load all three components simultaneously and thus excite interactions between them, allowing a full calibration on a 3×9 matrix. Calibration results were shown to agree with the factory calibration to within the expected repeatability of the balance (0.1-0.2% of full-scale measurement).

Particle Image Velocimetry System

The PIV laser sheet configuration for the fin vortex measurements in the TWT is shown in Fig. 3, in which stereoscopic PIV is used to obtain all three velocity components in the wind tunnel crossplane. The laser sheet was aligned normal to the wind tunnel axis and positioned to the midpoint of the test section side-wall window. The coordinate system is chosen such that the u component lies in the streamwise direction and the v component is in the vertical direction, positive away from the top wall; the w component is chosen for a right-handed coordinate system. The origin is located at the trailing edge of the fin root in its zero angle-of-attack position, regardless of its position along the test section axis.

The light source was a frequency-doubled dual-cavity Nd:YAG laser (Spectra Physics PIV-400) that produced about 400 mJ per beam. The beams were formed into coplanar sheets and directed into the test section from beneath the wind tunnel. To limit the particle dropout arising from the alignment of the freestream direction of the wind tunnel with the out-of-plane motion through the laser sheet, a relatively thick laser sheet of about 2 mm and brief time between pulses of 1.40 μs were employed.

The TWT is seeded by a thermal smoke generator (Corona Vi-Count 5000) that produces a large quantity of particles typically 0.2 - 0.3 μm in diameter from a mineral oil base. Particles are delivered to the TWT's stagnation chamber upstream of the flow conditioning section to eliminate disturbances associated with particle injection. *A*

posteriori analysis of the velocity data presented below derives a Stokes number on the order of 0.01, which indicates the particles are sufficiently small that they rapidly attain the local velocity and avoid particle lag biases even in the presence of velocity gradients due to the fin trailing vortex [6, 7].

Scattered laser light was collected by interline-transfer CCD cameras (Redlake MegaPlus ES4.0/E) with a resolution of 2048 × 2048 pixels digitized at 8 bits. The two cameras were equipped with 200 mm lenses mounted on Scheimpflug platforms to create an oblique focal plane aligned with the laser sheet. Both cameras looked through the same test section window, viewing the laser sheet from opposite directions, because placing one camera at the other side-wall window would have precluded access to the test section. The limited optical access additionally prevents meaningful movement of the crossplane location upstream or downstream; thus all data have been acquired at a single position within the test section. Different stations with respect to the fin were achieved by moving the fin's location. Stereoscopic camera calibrations used the multi-plane procedure described by Soloff et al. [8] to tie together the two sets of image pairs to produce three-dimensional vectors.

Data were processed using LaVision's DaVis v7.1, where image pairs were interrogated with a 64 × 64 pixel window employing two iterations with adaptive window offsets to account for the local particle displacement and incorporating image deformation based upon local velocity gradients, using a bilinear interpolation scheme to warp the images. A 50% overlap in the interrogation windows was used as well to oversample the velocity fields. The resulting vector fields were validated based upon signal-to-noise ratio, nearest-neighbor comparisons, and allowable velocity range. All vector fields shown in the present paper are mean data found from anywhere between a single wind tunnel run of 150 instantaneous samples and upwards of ten tunnel runs of 150 samples each; subsequent uncertainty estimates pertain to a single wind tunnel run and hence are conservative for all cases.

Experimental Conditions

Testing conditions have been selected to represent a portion of the range flown by transonic vehicles that may incorporate precision guidance capabilities. Limitations of the solid-wall test section restrict the maximum Mach number possible, but future studies will address true transonic flow very near Mach 1. For the present work, the nominal freestream Mach number is M_∞=0.5, 0.6, 0.7, and 0.8 with the wind tunnel stagnation pressure P_0 set to yield a test section static pressure p_w=101 kPa (14.7 psia). The wind tunnel air supply is heated in the storage tanks, but not temperature-controlled subsequent to this; therefore the freestream stagnation temperature T_0 is subject to minor variation from 316 K to 328 K (108 - 130°F).

The wall pressure p_w was measured from the mean of two static pressure taps located on the wind tunnel side walls 490 mm upstream of the laser sheet location, as seen in Fig. 3. M_∞ and the freestream velocity U_∞ were calculated isentropically from the ratio p_w/P_0 and the stagnation temperature T_0. The freestream Mach number rises with downstream distance due to boundary layer growth on the wind tunnel walls in the constant-area cross-section; hence, the actual Mach number at the fin location or laser sheet position will be greater than the nominal value established for the flow. To determine the local value, a series of pressure taps were installed in one side wall of the test section and recorded during every wind tunnel run. The greatest rise occurs at Mach 0.8, where an increase to Mach 0.834 is observed at the laser sheet position.
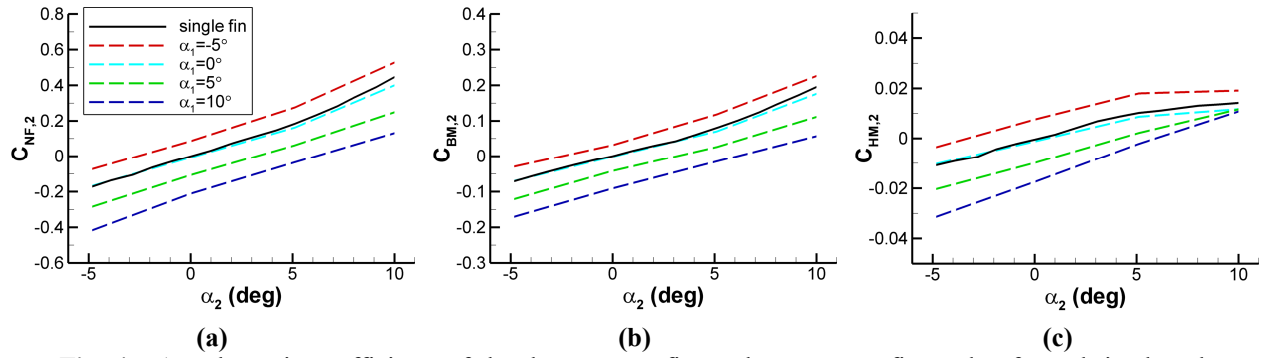
The 99%-velocity boundary layer thickness has been measured as 15.4 ± 0.4 mm (0.61 ± 0.02 inch) from PIV data acquired in the streamwise plane [9]. This measurement was made on the wind tunnel centerline at the same downstream position as the crossplane laser sheet.

Results and Discussion

Fin Aerodynamics

Data first were acquired using the fin balance on a single fin to obtain a baseline for fin performance free of aerodynamic interference from an upstream fin. Following this activity, the second fin was placed into the wind tunnel. The upstream and downstream fins were separated by a length of four fin root chords measured from fin center to fin center. The angle of the upstream fin, α_1, successively was set to four different angles, while the downstream fin angle, α_2, was cycled through different angles as well. The results are shown in Fig. 4 for the normal force coefficient C_{NF}, the bending moment coefficient C_{BM}, and the hinge moment coefficient C_{HM}. Coefficients are normalized by the dynamic pressure at the local Mach number (i.e., accounting for the increase due to boundary layer growth) and the fin planform area; the two moments are additionally normalized by the fin span or the average chord, respectively. The bending moment is referenced to the wind tunnel wall and the hinge moment to the fin root center point.

Figure 4 shows the alteration of the forces and moments on the downstream fin due to presence of the vortex shed from the fin tip of the upstream fin. The normal force, C_{NF}, essentially shifts above or below the single-fin data

Fig. 4: Aerodynamic coefficients of the downstream fin as the upstream fin angle of attack is altered. Single fin data are shown for comparison. (a) normal force; (b) bending moment; (c) hinge moment.

based upon the angle of attack of the upstream fin. In the case of no upstream fin cant, the data do not change significantly from the single-fin case, with slight deviation at the highest angles of attack for the downstream fin. This occurs because no vortex is generated when the upstream fin is aligned with the freestream, though a wake can be expected. As the upstream fin becomes canted, the additional effect of the generated vortex upon the downstream fin becomes evident, which appears to be largely constant across the range of downstream fin angles (this turns out to be accurate except at $\alpha_2=10°$). Behavior of the bending moment is virtually identical, but the hinge moment displays some convergence of the data at large downstream fin angle.

The effect upon the aerodynamic coefficients due to changing the freestream Mach number is given in Fig. 5. Data curves are plotted for nominal Mach numbers increasing from $M_\infty=0.5$ to 0.8, where deepening color and increasing line solidity denote higher Mach. A small increase in magnitude of the effect of the upstream shed vortex can be seen for the normal force and the bending moment, but for the hinge moment, an increase in Mach number actually reduces the coefficient magnitude. The effect is greatest when the upstream and downstream fins are pitched in opposite directions, suggesting that the leading edge of the downstream fin must be moved outside the position of the vortex core to create a meaningful Mach number influence. The relatively mild effect due to Mach number indicates that the increase in Mach number owing to boundary layer growth in the test section is not likely to be a significant factor in interpreting the data, when appropriately normalized.
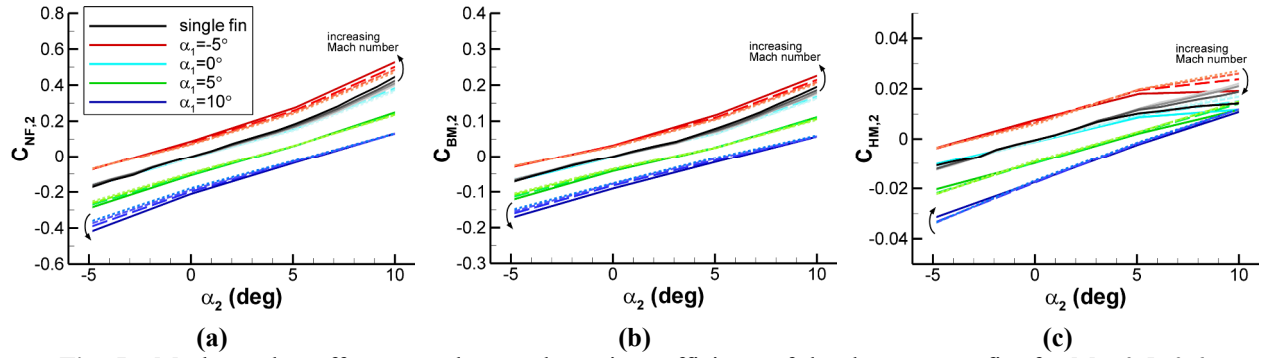
Finally, the effect due to the axial spacing between fins may be examined. This value, G, is expressed as the distance between fin centers and is normalized by the fin root chord c. Three values were tested, $G/c=2$, 3, and 4 (where $G/c=4$ was used for the data in Figs. 4 and 5) and are shown in Fig. 6, where deepening color and increased line solidity denote larger G. As would be anticipated, a decrease to the fin spacing enhances the interaction effect because the vortex, whose strength decays with downstream distance, is stronger when it reaches the second fin. The magnitude of this effect is dependent upon each fin angle, likely due to the position of the leading edge of the downstream fin within the vortex.

An uncertainty analysis for the aerodynamic data shows that the uncertainty is constant at about 0.1-0.2% of full-scale, including repeatability of the tunnel conditions, when normalized to obtain aerodynamic coefficients. Error bars, therefore, reach about twice the thickness of the lines plotted in Figs. 4-6, indicating that the uncertainties are consistently small and do not influence interpretation of the data presented. Further details concerning the uncertainty are found in Ref. 10.
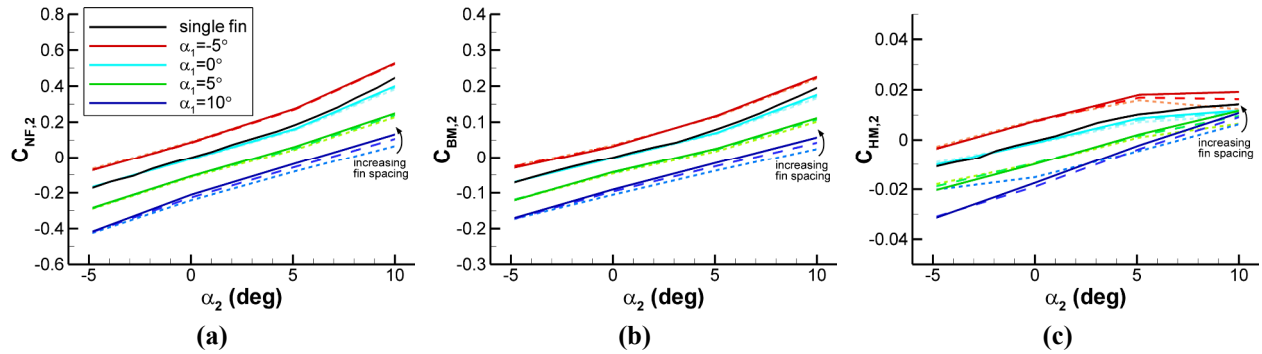
Fin Vortex Velocimetry

PIV data were acquired with only a single fin placed into the wind tunnel because the presence of the downstream fin would partially occlude the images. It is assumed that the same vortex shed from the upstream fin would impinge upon the downstream fin were it present; i.e., that no upstream influence occurs from the downstream fin.

Mean velocity data are shown in Fig. 7 for $M_\infty=0.8$ at five angles of attack of the single fin, $\alpha=0°$, 2°, 5°, 7°, and 10°. The fin was mounted as far upstream in the wind tunnel as possible, therefore placing the PIV measurement location at a distance of $x/c=4.18$ from the trailing edge of the fin, which corresponds to G/c=4.68 (although aerodynamics are usually referenced to the fin's pivot point, vortices are commonly measured from the trailing edge of the surface from which they originate). In-plane velocities are displayed as vectors superposed upon a contour plot of the out-of-plane (streamwise) velocities, with vectors subsampled by a factor of two in each dimension for visual clarity. The axes have been normalized to the fin root chord c and velocities by the freestream velocity as determined by the PIV data. All data are plotted on a common scale.

Fig. 5: Mach number effect upon the aerodynamic coefficients of the downstream fin, for M_∞=0.5, 0.6, 0.7, and 0.8. Single fin data are shown for comparison. (a) normal force; (b) bending moment; (c) hinge moment.

Fig. 6: Fin spacing effect upon the aerodynamic coefficients of the downstream fin, for G/c=2, 3, and 4. Single fin data are shown for comparison. (a) normal force; (b) bending moment; (c) hinge moment.

Figure 7 (in particular Figs. 7d and 7e) shows that the fin tip vortex is clearly visualized, both by the in-plane rotation and the out-of-plane streamwise velocity deficit. As the angle of attack is increased, the strength of the vortex increases markedly, seen in the magnitudes of both the in-plane velocity vectors and the streamwise velocity deficit. Although the α=0° case does not generate a vortex, a wake is still created, which would explain the small degree of aerodynamic interference observed in Fig. 4 when the downstream fin is at large angle of attack. A close study of Fig. 7 shows that the vortex position moves laterally further from the centerline as α is increased, though naturally it remains at a height roughly corresponding to the position of the fin tip. This lateral displacement exceeds the distance purely associated with the location of the fin trailing edge due to the fin cant.
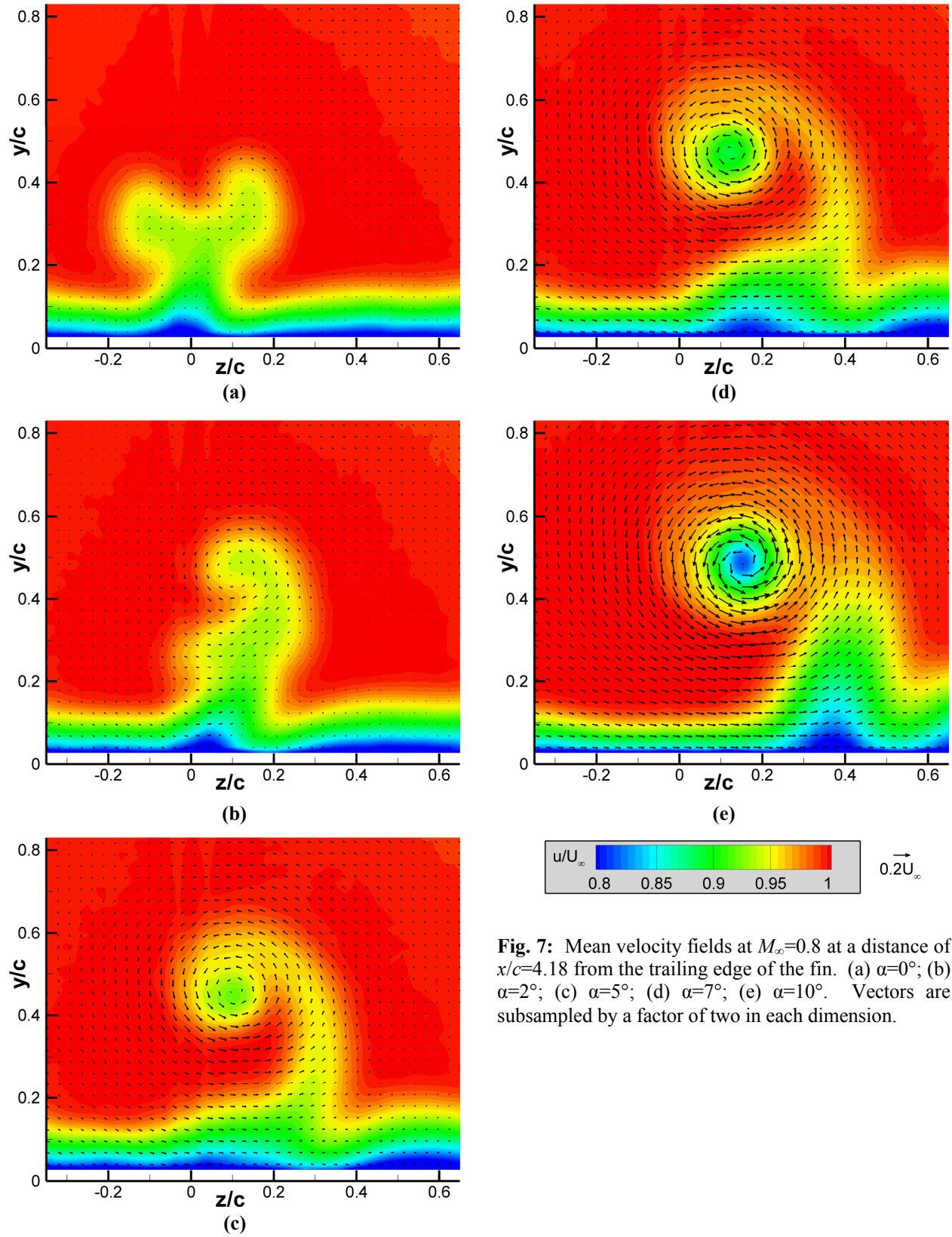
The fin trailing vortex itself is entirely analogous to the well-known wing tip vortices produced by aircraft, for which a wide range of velocimetry studies have been conducted (reviews are found in [11-14]). The same characteristic structure is observed here, including the presence of a primary vortex core with a thin vortex sheet continuing to spiral around the core (in the present case, additionally lifting the wall boundary layer) and the prominence of axial flow within the vortex core.

The Mach number effect upon the fin trailing vortex was examined at M_∞=0.5, 0.6, 0.7, and 0.8. When appropriately normalized, no difference can be discerned between the four Mach numbers tested, and hence the figures are omitted. Measurement of derived quantities such as the vortex circulation, centroid position, and size (see below) quantitatively support this observation. However, a subtle effect due to Mach number was detected by the fin balance measurements of the two-fin configuration in Fig. 5. This suggests that in fact vortex impingement on the downstream fin may have a secondary effect on the aerodynamics.

The downstream evolution of the vortex was studied by acquiring PIV data at the same station within the tunnel, as discussed earlier, but shifting the fin to a location closer to the laser sheet. This places the fin at a slightly higher Mach number because of the increase with downstream distance in the constant-area test section, but as mentioned above, when properly normalized, this effect can be expected to be negligible for such small changes in Mach number. Figure 8 plots the streamwise velocity field (out-of-plane) at four downstream positions, showing the gradual decrease in the magnitude of the velocity deficit with downstream distance, accompanied by an apparent increase in vortex size. Though not visible in the figure, the magnitude of the in-plane velocities associated with the
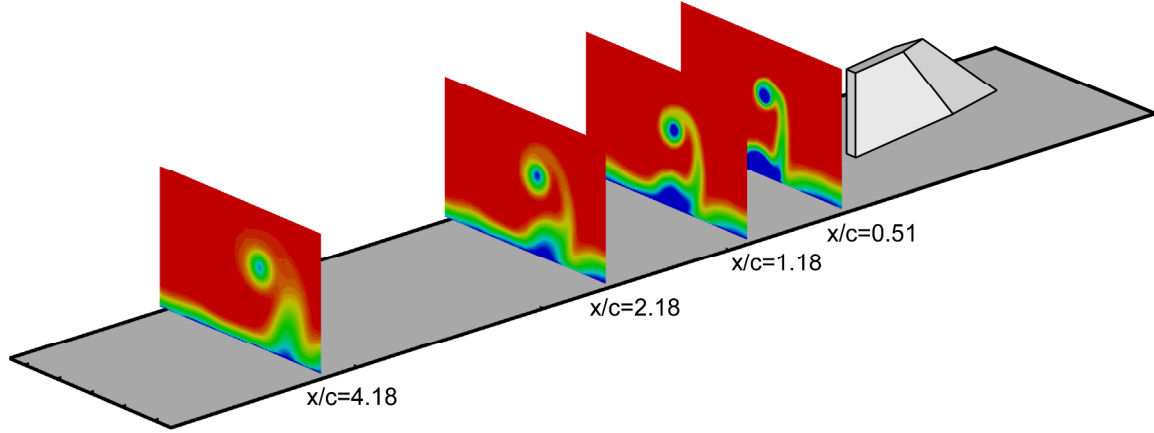
American Institute of Aeronautics and Astronautics

American Institute of Aeronautics and Astronautics

Fig. 7: Mean velocity fields at M_∞=0.8 at a distance of x/c=4.18 from the trailing edge of the fin. (a) α=0°; (b) α=2°; (c) α=5°; (d) α=7°; (e) α=10°. Vectors are subsampled by a factor of two in each dimension.
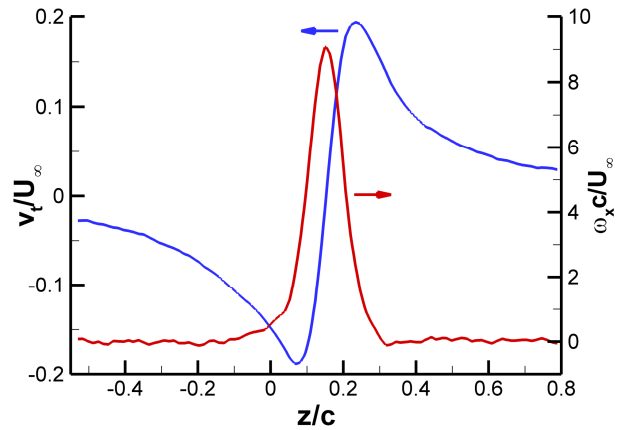
Fig. 8: Mean streamwise velocity field (out-of-plane) at four downstream locations for M_∞=0.8 and α=10°.

vortical rotation also decreases with downstream distance. Such measurements are useful for better understanding the underlying physics of the vortex shedding and for comparison with the aerodynamic effects of different fin spacing as plotted in Fig. 6.

The vortex properties may be reduced to singular values by defining the strength, size, and position of the vortex. The vortex strength most obviously is found from the circulation over some specified perimeter, then the vortex size and position readily follow from the area and centroid of that contour. Calculation of the required vorticity field is straightforward using a finite-difference scheme, but several options are available to demarcate the vortex boundary over which to integrate the circulation. Definition of the vortex core has wide agreement in the open literature, where the contour is given by the point of maximum tangential velocity of the vortex at each angular position, over which integration yields the vortex core circulation Γ_c. Figure

Fig. 9: Vortex tangential velocity (blue) and vorticity (red) extracted from Fig. 7e along a horizontal line through the vortex centroid.

9 shows a horizontal cut through the centroid of the vortex measured at conditions α=10°, M_∞=0.8, and x/c=4.18 (Fig. 7e), providing both the tangential velocity and the vorticity profile. A quick examination of either this plot or those of Fig. 7 reveals that this definition of the vortex core neglects a substantial portion of the vorticity, therefore it is desirable to define a second, larger vortex perimeter. The most common approach is that of Hoffman and Joubert [15], where, by analogy with the 99%-velocity boundary layer thickness, the contour is extended until the integration provides a circulation equivalent to 99% of the total circulation. In practice, however, this performs poorly in experimental data because measurement noise interferes with the integration long before the 99% boundary is reached, a difficulty noted in other experiments [15-17] and found to occur with the present data despite having averaged over a large number of individual PIV samples to obtain the clean appearance of Figs. 7-9. However, the results discussed subsequently are found not to be dependent upon the contour definition, so this outer contour may safely be ignored and just the vortex core studied. Much additional insight into the development of the vortex and its physical properties can be gleaned from these properties, but such analysis will be provided in a future publication whereas the present work focuses upon the vortex properties and their relationship with the interaction aerodynamics imposed on the downstream fin.

The uncertainty of the PIV measurements can be separated into precision and bias components. Determining the precision error is straightforward by analyzing repeated wind tunnel runs for the M_∞=0.8, α=10°, x/c=4.18 test conditions, from which the precision uncertainty is found to be about 2 m/s in each velocity component, including repeatability of the tunnel conditions from one run to another. Estimating the bias error due to the camera calibration (i.e., registration error) is more challenging. The calibration bias was found by reinstating the calibration target into the measurement location and traversing it a known distance in two dimensions corresponding to the

American Institute of Aeronautics and Astronautics

expected particle motion in the time between laser pulses, then processing the resulting images as if they were PIV data. Bias values were found from the deviation of the measured translation with the actual motion, yielding a bias of about 4 m/s, which is at the limit of accuracy of positioning and translating the calibration target. The total uncertainty, then, is about 5 m/s, equating to $0.02U_\infty$, in each velocity component.
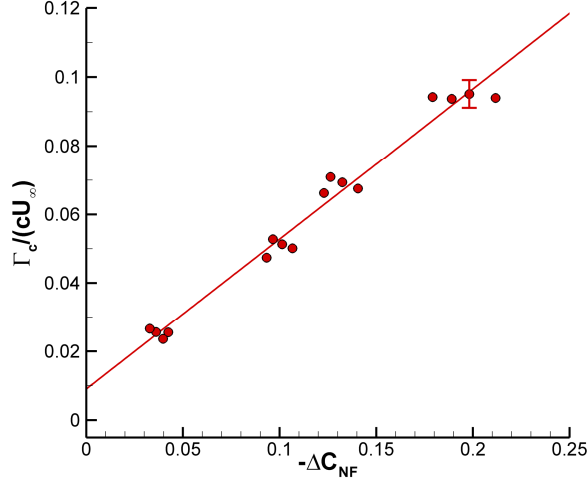
Data Correlation

Given that the fin trailing vortex visualized using PIV is responsible for the aerodynamic effects measured by the fin balance, a correlation between the two measurements would be anticipated. To examine this notion, the PIV data were reduced to a single representative value, the vortex core circulation Γ_c, and plotted in Fig. 10 against ΔC_{NF}, the change in the normal force coefficient due to the interaction, as compared to the single fin value. All Mach numbers and fin angles are plotted together, and a linear trendline is displayed. As is clearly seen, a strong correlation is found. Since Fig. 7 shows that the position of the vortex shifts only mildly with a change in the upstream fin angle, it is logical that the vortex strength would be the dominant parameter driving the interaction. The data points congregate into four groups representing data from α=2, 5, 7, and 10°; α=0° is omitted because no vortex is found at this condition. The horizontal spread in each cluster arises from the Mach number influence present in the balance measurements (see Fig. 5) but not in the PIV data. Data points are shown just for the PIV measurements at x/c=4.18 and are plotted against ΔC_{NF} values from the balance data of x/c=3.5 (G/c=4). The relatively small influence of fin spacing upon the balance data (Fig. 6) suggests that the mismatch between PIV and balance positions is of minor significance. Use of the PIV data at x/c=4.18 produces the lowest-noise correlations because the most PIV samples were incorporated into the mean velocity fields at this station, but results are similar when plotting Γ_c from the x/c=2.18 PIV measurement plane against balance measurements interpolated between the x/c=1.5 and x/c=2.5 fin spacings. Results also are similar using ΔC_{BM} or ΔC_{HM} instead. The error bars are estimated from the scatter between repeated measurements at M_∞=0.8, α=10°, and x/c=4.18.
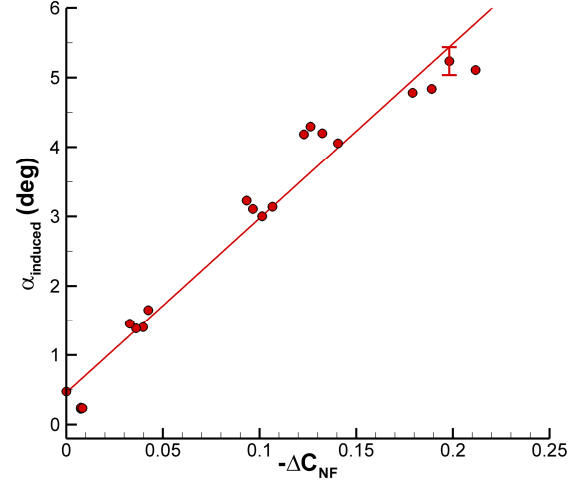
Because the vortex circulation is a quantity integrated from the velocity field, this suggests that a more fundamental relationship with the aerodynamic properties can be found in the velocities generated by the fin trailing vortex. This possibility is examined by extracting from each PIV field the mean velocity vector along the fin span as if the downstream fin had been installed at the laser sheet location at α=0°. From this velocity vector, the induced angle of attack upon the fin, $\alpha_{induced}$, may be calculated. This value is plotted against ΔC_{NF} in Fig. 11 for the same PIV and balance stations as Fig. 10, x/c=4.18 and 3.5, respectively. Again, a clear correlation is evident, and similar results are found at the other laser sheet locations or instead using ΔC_{BM} or ΔC_{HM}. These results are consistent with a previous study of the aerodynamic origins of jet/fin interaction, in which the vortices produced by the interaction of the exhausting jet with the freestream create an induced angle of attack on a downstream fin to alter its roll torque [18].

Still, Fig. 11 compares two distinctly different types of data. An improved comparison can be sought by converting $\alpha_{induced}$ to a normal force coefficient using the single-fin balance data such as given in Fig. 12, which provides the relevant aerodynamics of the fin as a function of its angle of attack. This yields the normal force coefficient of the interaction as inferred from the PIV velocity field, $\Delta C_{NF,piv}$, which is distinct from that directly measured by the balance, $\Delta C_{NF,balance}$. These two values are plotted against each other in Fig. 13, which shows that they lie very close to the ideal one-to-one correspondence given by the broken black line; only those data points for α=10° lie beyond the measurement uncertainty, and not by much. The agreement between ΔC_{NF} found by either the balance or the velocity field suggests that the alteration in the fin aerodynamics is indeed a result of an angle of attack induced upon the downstream fin by the rotational motion of the vortex shed from the upstream fin.
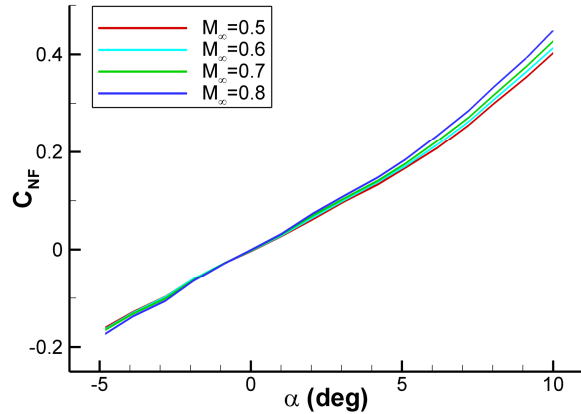
Though no trend of $\alpha_{induced}$ with Mach number is suggested by each cluster of data points in Fig. 11, once converted to $\Delta C_{NF,piv}$ in Fig. 13, the data points develop a slope consistent with the ideal correspondence line. That is, $\alpha_{induced}$ is not a function of the freestream Mach number, but $\Delta C_{NF,piv}$ is a weak function of Mach number. This is easily understood by examining plots of C_{NF} for a single fin in Fig. 12 that were used to convert $\alpha_{induced}$ to $\Delta C_{NF,piv}$. Here, the Mach number trend is evident as the angle of attack increases. Assembling all these data, the PIV measurements show that there is no Mach number dependence found in the structure of the vortex shed from a fin, but a Mach number dependence does arise as the downstream fin reacts to the angle of attack induced by the impinging vortex. This accounts for the Mach number effect seen in Fig. 5, and supports the claim that the underlying fluid dynamics of the interaction may be understood even with the downstream fin removed from the PIV experiment. Most likely, the Mach number influence upon the fin aerodynamics is a result of the vortex lift generated at the swept leading edge of the fin. Polhamus's theory shows a moderate increase in vortex lift on a delta wing as the freestream Mach number rises towards sonic conditions [19], and the same trend is indicated by Lamar's extension of this theory to cropped delta wings resembling the current fin geometry [20]. Additional support may be found in Longo's Euler simulations of delta wing flow [21].
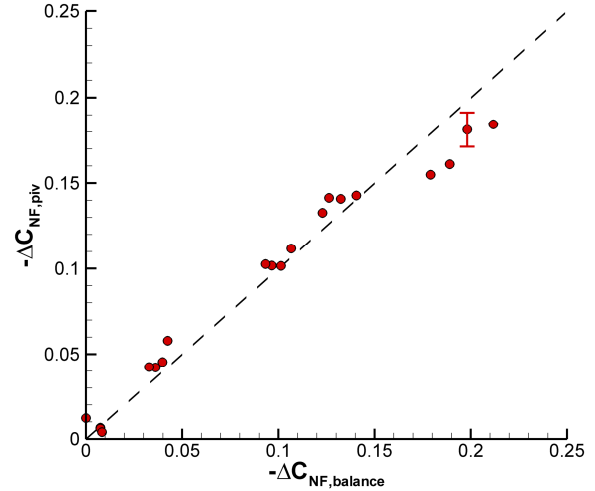
Fig. 10: Correlation of vortex core circulation derived from the PIV velocity field with the change in the normal force coefficient due to the interaction. Data shown at x/c=4.18.

Fig. 11: Correlation of the angle of attack upon a downstream fin induced by the vortex rotation with the change in the normal force coefficient due to the interaction. Data shown at x/c=4.18.

Fig. 12: Normal force coefficient measured by the aerodynamic balance for a single-fin configuration.

Fig. 13: Normal force coefficient due to the interaction as measured by the aerodynamic balance compared to the same value as inferred from the PIV measurements. Data shown at x/c=4.18.
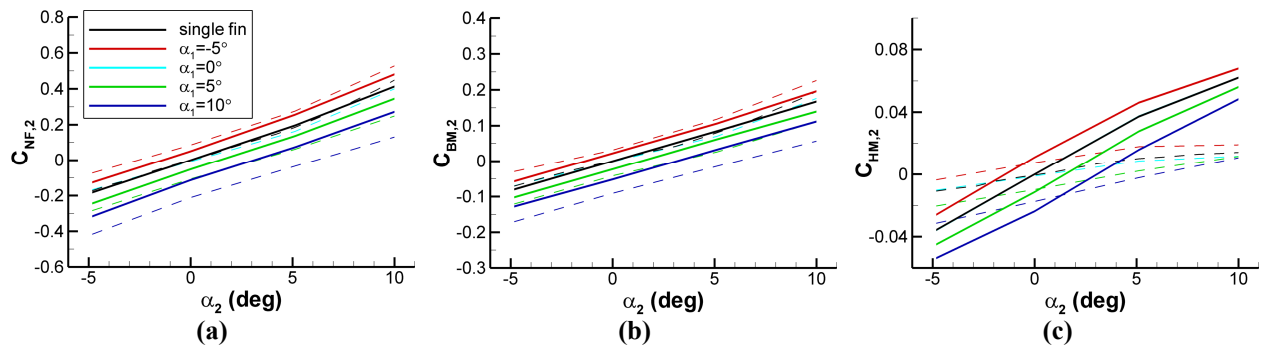
A stronger test of the theory that the fin-wake interaction is simply a result of the induced angle of attack from the trailing vortex can be performed by creating experimental configurations that place the vortex into different locations with respect to the downstream fin. For example, a flight vehicle at angle of attack will move the trailing vortex generated by the forward fin laterally relative to the downstream fin because the vortex trajectory will follow the freestream direction, whereas the current wind tunnel experiment is confined to a body angle of attack of 0°. To expand the experimental configuration, additional insert blocks were fabricated that shift the fins off the wind tunnel centerline and allow testing at fin positions corresponding to different vehicle angles of attack. This will produce aerodynamic data that complement Figs. 10, 11, and 13 by directing the vortex to impinge upon the downstream fin at a different position, as opposed to the single vortex position possible thus far. Such additional data will more robustly examine the relationship suggested by Figs. 11 and 13, although this approach will not replicate the fin-body interaction at angle of attack found on actual missile bodies (for example, Ref. 22). These experiments are underway at the time this document is being written, but unfortunately results will have to wait until a future publication.
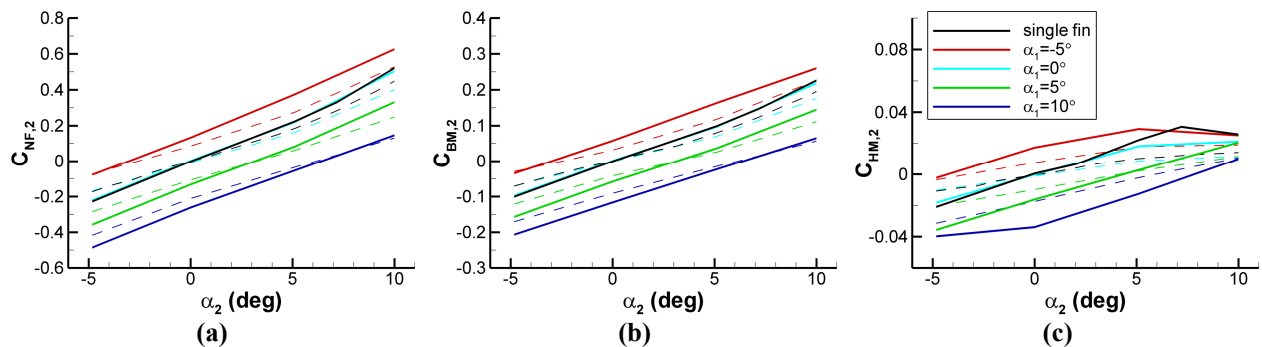
Computational Comparisons

Both the balance data and the PIV measurements can be used to assess the performance of common engineering software tools for predicting the effects of fin-wake interactions. Missile DATCOM [1] is one of the most widespread codes used to design bombs and missiles due to its ease of use and rapid results, but it is intended for application to axisymmetric bodies rather than the current flat plate configuration. To address this, a Missile DATCOM body was created based upon an ogive cylinder with a nose length of 3.05 m (120 in), a cylinder length of 6.1 m (240 in), and body diameter of 3.05 m (120 in). The fin was placed 7.6 m (300 in) from the nosetip, effectively beyond the influence of the nose. Compared with a fin root chord of 76 mm (3 in), this essentially simulates a flat plate. These body parameters were modified widely and found to have minimal effect on the predicted fin forces, establishing that the body influence upon the fin(s) has been minimized. Mach number and Reynolds number were set identical to the experimental conditions in the TWT and no attempt was made to simulate the tunnel wall boundary layer.

Missile DATCOM aerodynamic interference results for two fins separated by $G/c=4$ and at $M_\infty=0.8$ are shown in Fig. 14, mimicking the experimental conditions of Fig. 4. The solid lines show the DATCOM predictions whereas the broken lines give the corresponding experimental results. Figure 14 demonstrates that DATCOM does a reasonable job of predicting the interaction trends for C_{NF} and C_{BM}, but obviously performs poorly for C_{HM}. Although the trends with respect to α_2 are well reproduced by DATCOM for C_{NF} and C_{BM}, the results with respect to α_1 are underpredicted; that is, the DATCOM curves are clustered closer together than the experimental data. The exaggeration of the C_{HM} effect represents the most distinct deficiency of DATCOM. Nevertheless, Missile DATCOM does a surprisingly reasonable job reproducing the experimental interaction aerodynamic trends given the relative simplicity of the physics incorporated into its algorithms.

Simulations also were conducted using Splitflow [23] in Euler mode. In this case, the true flat plate geometry is easily created inside a bounding geometry sufficiently large that no significant effect was detected due to the computational boundary. A symmetry (slip) boundary condition was set for the simulated wind tunnel wall and all other boundaries were established at freestream conditions based upon wind tunnel data. The initial grid has 75,000 points for the simulated volume and is refined automatically by the solver to approximately 300,000 grid points by

Fig. 14: Aerodynamic coefficients of the fin interaction. Solid lines show Missile DATCOM predictions and broken lines show the corresponding experimental data from Fig. 4. (a) normal force; (b) bending moment; (c) hinge moment.

Fig. 15: Aerodynamic coefficients of the fin interaction. Solid lines show Splitflow Euler predictions and broken lines show the corresponding experimental data from Fig. 4. (a) normal force; (b) bending moment; (c) hinge moment.

American Institute of Aeronautics and Astronautics

completion. A typical simulation required about 1000 iterations for good convergence of the force data (about an hour of computational time).
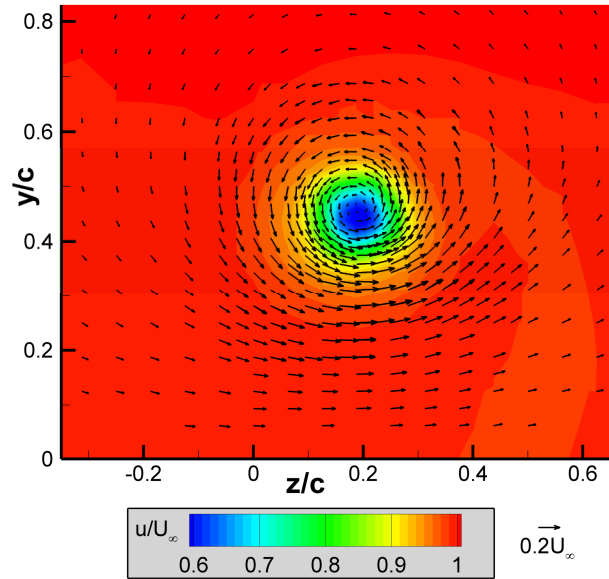
Figure 15 displays the data analogous to Fig. 14 but instead for the Splitflow Euler computations. As with Missile DATCOM, Splitflow does a good job predicting the trends for C_{NF} and C_{BM} as a function of α_2, but does a superior job to DATCOM in predicting the magnitude of the trends with regard to α_1. Furthermore, the Euler simulations are much more successful at predicting the C_{BM}.

A plot of the Euler simulation of the velocity field at x/c=4.18 for the M_∞=0.8, α=10° case is shown in Fig. 16, whose experimental analogue is in Fig. 7e. The vortex center is located slightly closer to the wall in comparison to the experimental data, by about $0.02c$, and is further outboard than the experiment by $0.04c$. The simulated axial velocity deficit is considerably greater than the experimental data, but the in-plane rotational velocity magnitudes appear well predicted, though of course the boundary layer effects found in the data are not reproduced by the Euler simulation. However, a close examination of the in-plane velocity field reveals that peak tangential velocity occurs further from the vortex center than is the case for the experiment in Fig. 7e. This becomes evident by comparing the vorticity fields of the experimental data and the Euler simulation in Fig. 17, where the simulated vortex is shown to be appreciably more diffuse with a lower peak vorticity magnitude. From this cursory look at the Splitflow Euler simulations, the vortex is not accurately represented, but curiously, it nevertheless reasonably reproduces the aerodynamic coefficients of the interaction (Fig. 15).
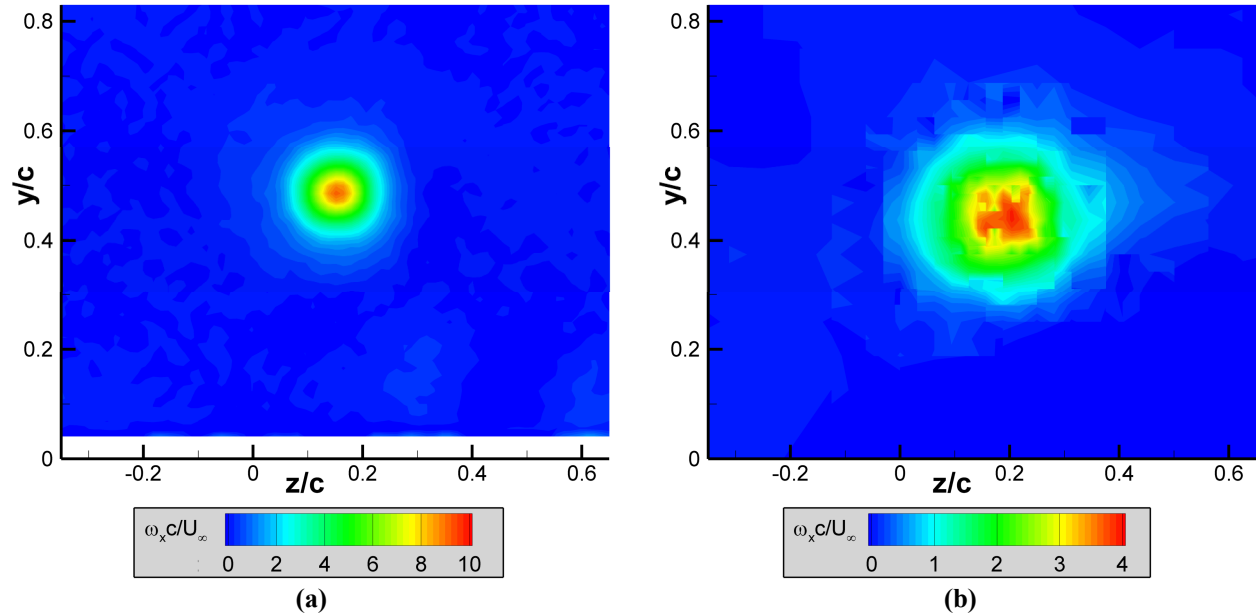
Higher fidelity CFD codes have not yet been examined using the present data.

Conclusion

To initiate a research program into fin trailing vortices and their aerodynamic influence upon downstream control surfaces, a sub-scale experiment has been constructed using fins mounted on one test section wall of a transonic wind tunnel. Data are

Fig. 16: Splitflow Euler simulation of the mean velocity field at M_∞=0.8, α=10°, and x/c=4.18.

Fig. 17: Vorticity plots for M_∞=0.8, α=10°, and x/c=4.18. (a) experimental data from Fig. 7e; (b) Splitflow Euler simulation from Fig. 16.

collected using two primary diagnostics, a fin balance mounted on the downstream fin to measure the aerodynamic forces of the interaction, and stereoscopic Particle Image Velocimetry (PIV) to measure the properties of the vortex responsible for the interaction.

The fin balance data show that the aerodynamic coefficients characterizing the downstream fin essentially are shifted above or below the baseline single-fin data dependent upon the angle of attack of the upstream fin. Freestream Mach number and the spacing between fins have secondary effects. The fin vortex velocimetry shows that the vortex strength increases markedly with upstream fin angle of attack, though even an uncanted fin generates a noticeable wake. No variation with Mach number can be discerned in the normalized velocity data, but data taken at progressively further stations following the fin trailing edge show the decay in vortex strength with downstream distance. Correlations between the force data and the velocimetry suggest that the interaction is fundamentally a result of an angle of attack superposed upon the downstream fin by the vortex shed from the upstream fin tip. The Mach number influence arises from differing vortex lift on the leading edge of the downstream fin even when the impinging vortex is Mach invariant. The analysis supports the argument that the aerodynamic response of the downstream fin can be determined without considering vortex breakdown on the fin.

Numerical predictions of the interaction were examined using Missile DATCOM and Splitflow Euler simulations. Missile DATCOM performed reasonably when predicting the interaction trends for the normal force and the bending moments but functioned poorly for the hinge moment. The Euler computations performed somewhat better, in particular regarding the hinge moment, despite having simulated a distinctly larger vortex with a lower peak vorticity than that measured in the experiment.

References

[1]   Blake, W. B., "Missile DATCOM: User's Manual – 1997 Fortran 90 Revision," U.S. Air Force Research Lab/Air Vehicles Directorate, AFRL-VA-WP-TR-1998-3009, Wright-Patterson Air Force Base, OH, 1998.

[2]   Dillenius, M. F. E., Lesieutre, D. J., Hegedus, M. C., Perkins, S. C. Jr., Love, J. F., and Lesieutre, T. O., "Engineering-, Intermediate-, and High-Level Aerodynamic Prediction Methods and Applications," *Journal of Spacecraft and Rockets*, Vol. 36, No. 5, 1999, 609-620.

[3]   Mikhail, A. G., "Assessment of Two Fast Aerodynamic Codes for Guided Projectiles," *Journal of Spacecraft*, Vol. 24, No. 4, 1987, pp. 303-310.

[4]   Smith, E. H., Hebbar, S. K., and Platzer, M. F., "Aerodynamic Characteristics of a Canard-Controlled Missile at High Angles of Attack," *Journal of Spacecraft and Rockets*, Vol. 31, No. 5, 1994, pp. 766-772.

[5]   Sooy, T. J., and Schmidt, R. Z., "Aerodynamic Predictions, Comparisons, and Validations Using Missile DATCOM (97) and Aeroprediction 98 (AP98)," *Journal of Spacecraft and Rockets*, Vol. 42, No. 2, 2005, pp. 257-265.

[6]   Samimy, M., and Lele, S. K., "Motion of Particles with Inertia in a Compressible Free Shear Layer," *Physics of Fluids A*, Vol. 3, No. 8, 1991, pp. 1915-1923.

[7]   Melling, A., "Tracer Particles and Seeding for Particle Image Velocimetry," *Measurement Science and Technology*, Vol. 8, No. 12, 1997, pp. 1406-1416.

[8]   Soloff, S. M., Adrian, R. J., and Liu, Z-C, "Distortion Compensation for Generalized Stereoscopic Particle Image Velocimetry," *Measurement Science and Technology*, Vol. 8, No. 12, 1997, pp. 1441-1454.

[9]   Beresh, S. J., Henfling, J. F., Erven, R. J., and Spillers, R. W., "Penetration of a Transverse Supersonic Jet into a Subsonic Compressible Crossflow," *AIAA Journal*, Vol. 43, No. 2, 2005, pp. 379-389.

[10] Smith, J. A., Henfling, J. F., Beresh, S. J., Grasser, T. W., and Spillers, R. W., "A Three-Component Balance System for Measuring Forces and Moments in Fin-Wake Interactions," AIAA Paper 2007-5319, July 2007.

[11] Lee, G. H., "Trailing Vortex Wakes," *Aeronautical Journal*, Vol. 79, 1975, pp. 377-388.

[12] Hoeijmakers, H. W. M., "Vortex Wakes in Aerodynamics," AGARD CP-584: The Characterization and Modification of Wakes from Lifting Vehicles in Fluid, 1996, pp. 1-1 to 1-12.

[13] Spalart, P. R., "Airplane Trailing Vortices," *Annual Review of Fluid Mechanics*, Vol. 30, 1998, pp. 107-138.

[14] Jacquin, L., "On Trailing Vortices: A Short Review," *International Journal of Heat and Fluid Flow*, Vol. 26, No. 6, 2005, pp. 843-854.

[15] Hoffmann, E. R., and Joubert, P. N., "Turbulent Line Vortices," *Journal of Fluid Mechanics*, Vol. 16, No. 3, 1963, pp. 395-411.

[16] Corsiglia, V. R., Schwind, R. G., and Chigier, N. A., "Rapid-Scanning, Three-Dimensional Hot-Wire Anemometer Surveys of Wing-Tip Vortices," *Journal of Aircraft*, Vol. 10, No. 12, 1973, pp. 752-757.

[17] Shekarriz, A., Fu, T. C., Katz, J., and Huang, T. T., "Near-Field Behavior of a Tip Vortex," *AIAA Journal*, Vol. 31, No. 1, 1993, pp. 112-118.

[18] Beresh, S. J., Heineck, J. T., Walker, S. M., Schairer, E. T., and Yaste, D. M., "Planar Velocimetry of Jet/Fin Interaction on a Full-Scale Flight Vehicle Configuration," *AIAA Journal*, Vol. 45, No. 8, 2007, pp. 1827-1840.

[19] Polhamus, E. C., "Predictions of Vortex-Lift Characteristics by a Leading-Edge Suction Analogy," *Journal of Aircraft*, Vol. 8, No. 4, 1971, pp. 193-199.

[20] Lamar, J. E., "Prediction of Vortex Flow Characteristics of Wings at Subsonic and Supersonic Speeds," *Journal of Aircraft*, Vol. 13, No. 7, 1976, pp. 490-494.

[21] Longo, J. M. A., "Compressible Inviscid Vortex Flow of a Sharp Edge Delta Wing," *AIAA Journal*, Vol. 33, No. 4, 1995, pp. 680-687.

[22] Nielsen, J. N., "Missile Aerodynamics – Past, Present, Future," *Journal of Spacecraft*, Vol. 17, No. 3, 1980, pp. 165-176.

[23] Karman, S. L., "SPLITFLOW: A 3D Unstructured Cartesian/Prismatic Grid CFD Code for Complex Geometries," AIAA Paper 95-0343, January 1995.